TYPE Original Research
PUBLISHED 02 December 2025
DOI 10.3389/feart.2025.1715960



OPEN ACCESS

EDITED BY Haijun Qiu, Northwest University, China

REVIEWED BY
Linjuan Xu,
Yellow River Institute of Hydraulic
Research, China
Na He,
Henan Polytechnic University, China

*CORRESPONDENCE
Biao Yang,

☑ yangbiao50031@163.com

RECEIVED 30 September 2025 REVISED 23 October 2025 ACCEPTED 23 October 2025 PUBLISHED 02 December 2025

CITATION

Deng K, Yang B, Yu Z, Pu Q and He L (2025) Automatic extraction algorithm for landslide cracks using Insar-UAV LiDAR point cloud coupling.

Front. Earth Sci. 13:1715960. doi: 10.3389/feart.2025.1715960

COPYRIGHT

© 2025 Deng, Yang, Yu, Pu and He. This is an open-access article distributed under the terms of the Creative Commons Attribution License (CC BY). The use, distribution or reproduction in other forums is permitted, provided the original author(s) and the copyright owner(s) are credited and that the original publication in this journal is cited, in accordance with accepted academic practice. No use, distribution or reproduction is permitted which does not comply with these terms.

Automatic extraction algorithm for landslide cracks using Insar-UAV LiDAR point cloud coupling

Kailun Deng¹, Biao Yang²*, Zhilong Yu³, Quan Pu¹ and Linju He¹

¹State Key Laboratory of Geohazard Prevention and Geoenvironment Protection, Chengdu University of Technology, Chengdu, China, ²Southwest Company of China Airport Planning and Design Institute Co., Ltd., Chengdu, China, ³Chengdu Engineering Consulting Co., Ltd., Chengdu, China

In response to the bottleneck problems of weak landslide crack morphology, hidden features, and limited extraction accuracy in complex terrain masking and dense vegetation coverage environments, as well as the shortcomings of existing methods in cross scale and multi-source heterogeneous data fusion, this study proposes an automatic landslide crack extraction algorithm based on InSAR and UAV LiDAR point cloud collaboration. This algorithm relies on SBAS InSAR technology to achieve large-scale, long-term surface deformation monitoring, and identifies landslide deformation active areas through deformation rate threshold division and spatial clustering. In terms of fusion mechanism, a combination of control point matching and ICP (Iterative Closest Point) algorithm is adopted to accurately register the deformation zone data obtained by InSAR monitoring with the point cloud data obtained by UAV LiDAR, achieving effective fusion of cross scale and multi-source heterogeneous data. On this basis, guide the UAV LiDAR to conduct targeted fine scanning and obtain high-resolution 3D point cloud data. Based on point cloud, a three-dimensional model of landslide crack development area is constructed, and multidimensional morphological features such as width, direction, slope, and curvature are extracted. Discriminant feature vectors are constructed, and a probabilistic neural network (PNN) model is introduced to achieve probability classification of crack pixels through Gaussian kernel density estimation and Bayesian decision mechanism. Finally, edge extraction is optimized by Canny operator to achieve automated and high-precision recognition of crack contours. Fifty independent test cases were selected for the experiment, covering various types of landslides such as shallow soil landslides and rock landslides. The results showed that the proposed method performed well in multi vegetation covered environments, with IoU stability above 0.94, significantly better than existing mainstream methods, and had good robustness and engineering applicability.

KEYWORDS

InSAR, UAV lidar, deformation rate, landslide cracks, automatic extraction, probabilistic neural network

1 Introduction

Landslides are among the most common and highly destructive geological hazards worldwide, with their destabilization processes often accompanied by the initiation, propagation, and breakthrough of surface cracks (Yunus et al., 2025). These cracks serve as critical early indicators of slope instability (Sari et al., 2024), reflecting not only internal stress adjustments and deformation concentration within the slope body but also providing vital evidence for delineating potential landslide areas and predicting disaster trends (Yamaguchi and Kasai, 2022). Therefore, achieving early, precise identification and dynamic monitoring of landslide cracks is of paramount importance for establishing a geological disaster prevention and mitigation system (Ozturk, 2022).

However, traditional landslide crack monitoring methods (such as manual field inspections and ground surveys) suffer from low efficiency, limited spatial coverage, and high subjectivity, making them ill-suited to meet the demand for high-precision, realtime acquisition of crack information in complex terrain and vegetation-covered conditions (Mahesh et al., 2023). Particularly in areas with significant topographic undulations and dense vegetation, where fracture morphology is subtle and spatial characteristics are concealed, the applicability and reliability of traditional methods are significantly reduced (Tebbouche et al., 2022). In recent years, with the advancement of remote sensing technology, numerous scholars have attempted to incorporate machine learning and remote sensing image analysis methods to achieve automated identification of landslide fractures. For instance, Khadka et al. (2025) combined multi-source geographic features with a random forest model to identify landslide areas, but this method has limited capability to capture complex nonlinear relationships among features. Lekshmanan and George (2023) proposed a crack identification method based on Generative Adversarial Networks (GANs), yet it is prone to pattern collapse, resulting in insufficient diversity of generated samples. Yang et al. (2025) employed short-time Fourier transform for frequencydomain feature analysis, yet exhibited weak responsiveness to slow-creeping landslides and tended to overlook deep-seated fracture information (Shameem et al., 2022) utilized SVM models for susceptibility zoning, but their cross-regional generalization capability was poor, struggling to address challenges posed by geological environmental variations. Overall, existing methods predominantly rely on single data sources or isolated models, failing to effectively integrate multi-scale, multi-temporal remote sensing information. Particularly in complex environments with terrain occlusion and vegetation interference, extraction accuracy and robustness remain unsatisfactory.

InSAR technology possesses the capability for large-scale, high-precision, long-term surface deformation monitoring, becoming a crucial tool for early landslide detection (Tiwari et al., 2024). However, its effectiveness is constrained by side-view geometry, atmospheric delay, and vegetation penetration, often resulting in monitoring blind spots and signal decoherence in steep terrain or areas with high vegetation coverage (Diels et al., 2022). UAV LiDAR technology can actively acquire high-precision 3D point clouds, clearly revealing micro-topography, but lacks temporal monitoring capabilities, making it difficult to directly reflect the dynamic deformation process of landslides (Devaraj et al., 2022).

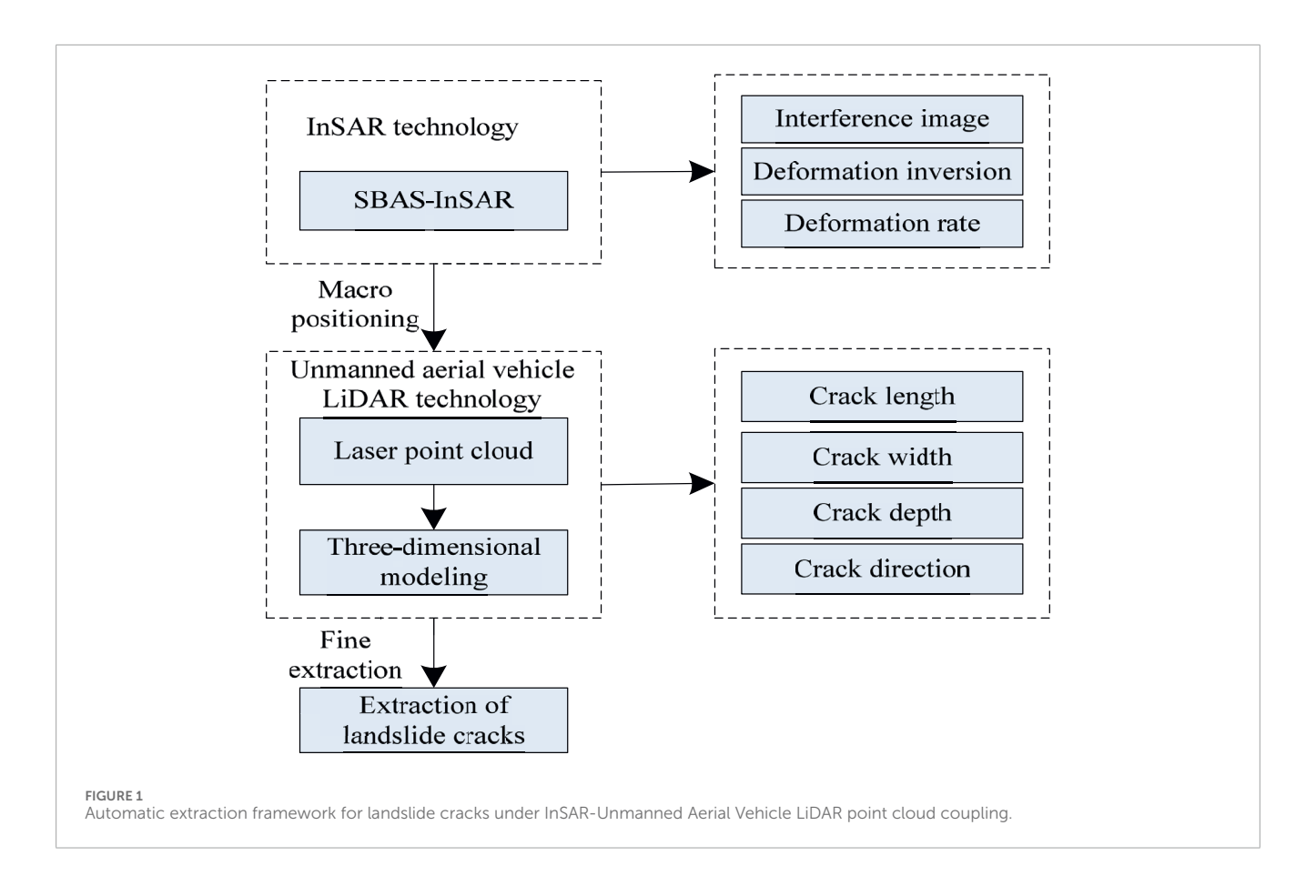
Consequently, no single technology can comprehensively meet the demands of landslide crack extraction. To address these challenges, this paper proposes an automated landslide crack extraction algorithm integrating InSAR and UAV LiDAR point clouds. By effectively coupling multi-source remote sensing data, it aims to resolve issues such as weak crack features, low extraction accuracy, and insufficient generalization capabilities of existing methods in complex environments. This approach fully leverages InSAR's macro-deformation monitoring capabilities and LiDAR's high-resolution 3D morphology capture. It incorporates a Probabilistic Neural Network (PNN) for feature fusion and fracture probability classification, achieving an integrated workflow from deformation-guided to detailed fracture extraction. This provides a novel technical pathway for early identification and monitoring/early warning of landslide hazards.

2 Automatic extraction of landslide cracks

2.1 Establishing an automatic extraction framework for landslide cracks

Landslide cracks are key precursor indicators of landslide instability. Due to their complexity, diversity, and limitations in monitoring environments (such as terrain obstruction and vegetation cover), a single technique struggles to comprehensively and accurately capture and extract all characteristic information of landslide cracks (Qiu et al., 2025). Therefore, this study couples InSAR and UAV LiDAR technologies. Specifically, InSAR's macrodeformation monitoring capability compensates for UAV LiDAR's limited monitoring range and difficulty in acquiring long-term deformation time series data. Conversely, UAV LiDAR's highresolution 3D detection advantage addresses InSAR's shortcomings in "insufficient micro-morphological characterization." Specifically: The deformation field provided by InSAR serves as prior knowledge to locate the active deformation zones (i.e., crack development areas) of the landslide, thereby guiding UAV LiDAR for detailed scanning and data processing in key regions. Subsequently, based on LiDAR point cloud information, the three-dimensional morphological features of cracks are extracted, enabling the automatic identification of landslide cracks. The coupling of these two technologies achieves complementary "deformation information + 3D morphological information," enabling precise, automated extraction of landslide cracks from 'surface' to "point" scale. This establishes an InSAR-UAV LiDAR point cloud coupled automatic landslide crack extraction framework, as shown in Figure 1.

Within the framework depicted in Figure 1, InSAR technology (SBAS–InSAR, Small Baseline Set Interferometric Synthetic Aperture Radar—an optimized InSAR method) is employed for macro-level positioning. Specifically, SBAS–InSAR monitors surface deformation rates across extensive areas for rapid identification of active deformation zones (landslide crack development areas). This provides clearly defined target regions for subsequent detailed detection, avoiding blind exploration and enhancing detection efficiency. After identifying landslide fracture zones, UAV LiDAR technology is employed for detailed extraction. This involves (1) acquiring high-precision laser point cloud data of the area



using UAV LiDAR, (2) performing 3D modeling to obtain threedimensional morphological characteristics of landslide fractures, and (3) analyzing this information with intelligent learning algorithms to achieve landslide fracture extraction.

2.2 Identification of active landslide deformation zones using SBAS-InSAR technology

SBAS-InSAR technology is a synthetic aperture radar (SAR) data processing method based on the principle of short spatiotemporal baseline interferometry. It achieves high-precision monitoring of ground deformation through multi-reference image timeseries analysis (Qadami et al., 2023). The fundamental approach to locating landslide deformation hotspots using SBAS-InSAR technology involves three key steps: constructing a small baseline set through multi-reference image time-series analysis; extracting high-precision surface deformation phase information via phase unwrapping and error correction techniques; and subsequently deriving surface deformation rates. Based on the spatial heterogeneity characteristics of deformation rates and combined with predefined thresholds, pixel-level screening and spatial clustering are employed to identify regions with anomalous deformation rates, enabling precise localization of landslide deformation hotspots (areas with developed landslide fractures).

The primary process for locating landslide deformation hotspots using SBAS-InSAR technology can be described as follows:

Data Preparation. Multi-scene terrain SAR images covering
the target monitoring area over a specific time frame
are collected via satellite active microwave remote sensing.
These images must possess sufficient overlap and span the
potential landslide activity period. Simultaneously, to ensure
continuity in the terrain SAR image time series, eliminate
geometric distortion and radiometric differences between
images, and guarantee that interferometric results accurately
reflect actual ground deformation, the SAR images are
arranged chronologically. Radiometric calibration and multiview processing are performed on each image.

In the preparation stage of SBAS InSAR data in this study, multi view processing adopts 5-view processing to improve image signal-to-noise ratio while also considering spatial resolution; The absolute calibration method is used for radiometric calibration. Based on the known radiometric characteristics of the calibration body, the grayscale values of SAR images are accurately converted into backscattering coefficients to ensure the uniformity and accuracy of radiometric levels between different images and ensure the reproducibility of research.

2. Reference Image Selection and Image Registration. To provide a stable baseline for subsequent interferometric processing and reduce cumulative registration errors across multi-period terrain SAR images, one scene is selected from all images as the "reference Image." This reference image must exhibit stable imaging conditions—such as minimal precipitation during acquisition, minimal vegetation cover changes, and a

moderate central viewpoint—positioned near the middle of the time series to ensure more uniform distribution of spatio-temporal baselines formed with other secondary images. After determining the reference image, all other images (secondary images) are registered to it, ensuring that the same geographic targets occupy identical pixel locations across all images. Registration is achieved through a geometric transformation model expressed as follows Equation 1:

$$(x_{master}, y_{master}) = \Upsilon(x_{slave}, y_{slave}; \zeta)$$
 (1)

In the formula, (x_{master}, y_{master}) and (x_{slave}, y_{slave}) represent the pixel coordinates of the reference and secondary images for the same target point, respectively. Υ denotes the transformation function, while ζ represents the transformation parameters (translation, rotation, and scaling coefficients).

3. Construction of the small baseline set (SBAS). Based on the registered images, combined with preset spatial baseline thresholds and temporal baseline thresholds, short-baseline interferometric pairs are filtered from all image pairs to form the small baseline set. The filtering criteria for interferometric pairs are as follows Equation 2:

$$|J_{\perp}| < J' and |\Delta T| < T' \tag{2}$$

where, J_{\perp} represents the vertical spatial baseline with a corresponding threshold of J', and ΔT represents the temporal baseline with a corresponding threshold of T'.

4. Generation of the interferogram. For each scene in the small baseline set, perform conjugate multiplication on the registered reference and secondary images to generate M differential interferograms I. The phase values in these interferograms contain information about terrain, deformation, atmospheric conditions, and noise in the target area, exhibiting entanglement (entanglement interval: $[-\pi, \pi]$). This is described by the formula as follows Equation 3:

$$I = S_{master} \cdot S_{slave}^* = \beta e^{j\phi_{wrapped}}$$
 (3)

Where, S_{master} and S_{slave} represent the complex pixel values of the reference and secondary images, respectively; * denotes the complex conjugate; β represents the interferometric amplitude; $\phi_{wrapped}$ denotes the wrapped interferometric phase. $\phi_{wrapped}$ is expressed as follows Equation 4:

$$\phi_{wrapped} = \Gamma \Big(\phi_{def} + \phi_{topo} + \phi_{atm} + \phi_{noise} \Big) \tag{4}$$

where, Γ denotes the wrapping operator, ϕ_{def} represents the deformation phase, ϕ_{topo} denotes the terrain phase, ϕ_{atm} denotes the atmospheric phase, ϕ_{noise} denotes the noise phase.

Through the above operations, series of reference-secondary image interferometric pairs are formed. The number of interferometric pairs M must satisfy the condition shown in Equation 5:

$$(N+1)/2 \le M \le N(N+1)/2$$
 (5)

where, N denotes the total number of terrain SAR images.

5. Phase unwrapping. Given that the interference phase of the interferogram exhibits periodic blurring 2π (with a wrapping interval of $[-\pi,\pi]$), it cannot directly reflect true surface deformation. Therefore, to obtain the true phase difference for accurate deformation rate calculation and subsequent deformation inversion, the wrapped interference phase $\phi_{wrapped}$ is restored to the true absolute phase $\phi_{unwrapped}$, described by the formula as follows Equation 6:

$$\phi_{unwrapped}(i,j) = \phi_{wrapped}(i,j) + 2\pi\varepsilon(i,j)$$
 (6)

In the equation, $\varepsilon(i,j)$ represents the integer-solved disentanglement order, which is the core unknown quantity to be solved for phase disentanglement. It must satisfy the continuity constraint of phase difference between adjacent pixels as follows Equations 7, 8:

$$\left|\phi_{unwrapped}(i,j) - \phi_{unwrapped}(i-1,j) - \Delta\phi_x(i,j)\right| \le \pi \tag{7}$$

$$\left|\phi_{unwrapped}(i,j) - \phi_{unwrapped}(i,j-1) - \Delta\phi_{y}(i,j)\right| \le \pi$$
 (8)

Where, $\Delta\phi_x(i,j)$ and $\Delta\phi_y(i,j)$ represent the phase difference between adjacent pixels.

In the process of phase unwrapping, to alleviate errors caused by atmospheric noise and other factors, the method of removing the atmospheric phase screen can be used. Firstly, estimate the atmospheric phase contribution based on external atmospheric data or by utilizing the characteristics of interferograms themselves. For example, by analyzing the phase change patterns at different time or spatial scales to separate atmospheric phase components, they can be subtracted from the unwrapped phase; Multiple image overlay averaging method can also be used to average the data using multiple sets of interferometers to reduce the influence of random atmospheric noise, thereby reducing the interference of phase unwrapping error on deformation rate calculation and improving the accuracy of deformation rate inversion.

6. Elimination of systematic errors. From the absolute phase after disentanglement, estimate and remove systematic error phases, primarily referring to terrain residual phases caused by elevation errors. The terrain residual phase model can be described as:

$$\phi_{tr} = \frac{4\pi}{\lambda} \cdot \frac{J_{\perp}}{R \sin \theta} \cdot \Delta h \tag{9}$$

where, ϕ_{tr} represents the terrain residual phase, λ denotes the radar wavelength, R signifies the slant range from the satellite to the ground target (i.e., the propagation distance of the radar signal), θ represents the radar wave incidence angle, Δh indicates the elevation error, which is the unknown quantity to be solved for in the model.

Solving Δh by least squares yields as follows Equation 10:

$$\Delta h = \operatorname{argmin}_{\Delta h} \sum \left| \phi_{unwrapped} - \frac{4\pi}{\lambda} \cdot \frac{J_{\perp}}{R \sin \theta} \cdot \Delta \tilde{h} \right|^{2}$$
 (10)

where, $\Delta \tilde{h}$ represents the parameter variable serving as the target during the solution process.

Substituting the obtained Δh into Equation 9 yields the terrain residual phase ϕ_{tr} . Subtracting this from $\phi_{unwrapped}$ produces the cleaned interferogram phase.

7. Deformation Inversion: Solve for the local deformation rate of the monitored area using. By establishing a mathematical relationship between deformation phase and deformation rate and solving it, deformation inversion is achieved from the purified interferogram phase information. This derives the linear deformation rate field of the monitored area's surface, enabling quantitative understanding of deformation velocity at different surface locations. This provides critical deformation data for subsequent identification of landslide deformation hotspots. Let the surface deformation rate be denoted as ρ and the time interval as Δt . The relationship between the deformation phase ϕ_{def} and ρ can be expressed as follows Equation 11:

$$\phi_{def} = (4\pi/\lambda)\rho \cdot \Delta t \tag{11}$$

For a small baseline set, with *M* interferometric pairs defined, a system of equations is constructed based on the phase data from multiple pairs—the core computational step in deformation inversion. Combining the deformation phase and deformation rate relationships for all interferometric pairs yields as follows Equation 12:

$$\begin{cases} \phi_{def,1} = (4\pi/\lambda)\rho \cdot \Delta t_1 \\ \phi_{def,2} = (4\pi/\lambda)\rho \cdot \Delta t_2 \\ \dots \\ \phi_{def,M} = (4\pi/\lambda)\rho \cdot \Delta t_M \end{cases}$$
 (12)

The above system of equations is solved using the least squares method to obtain the deformation rate ρ . The essence of the solution is to find a ρ that minimizes the sum of squared errors Z between the observed deformation phase and the theoretical deformation phase for all interferometric pairs. Define $Z = \sum_{i=1}^{M} \left(\phi_{def,i} - (4\pi/\lambda) \rho \cdot \Delta t_i \right)^2$. Setting the derivative of Z with respect to ρ to zero, i.e., $(dZ)/(d\rho) = 0$ leads to as follows Equation 13:

$$\sum_{i=1}^{M} 2 \left(\phi_{def,i} - (4\pi/\lambda) \cdot \rho \Delta t_i \right) \left(-(4\pi/\lambda) \Delta t_i \right) = 0$$
 (13)

After derivation, we obtain as follows Equation 14:

$$\rho_i = \left(\lambda \sum_{i=1}^M \phi_{def,i} \Delta t_i\right) / \left(4\pi \sum_{i=1}^M \Delta t_i^2\right)$$
 (14)

Through this computational process, the inversion from phase data to deformation rate is completed, yielding the deformation rate for each pixel in the monitored region.

8. Formative Mapping. Based on the deformation rate values of each pixel in the deformation rate field, different deformation rate values are mapped to different colors according to specific color mapping rules, generating a deformation rate map for the study area. Specifically, the deformation rate range is set to $[\rho_{min}, \rho_{max}]$, divided into several intervals, with each interval corresponding to a specific color. Each pixel is assigned the color corresponding to the interval containing its deformation rate value, resulting in a color image depicting the deformation rate distribution.

Through the mapping relationship between pixel coordinates and geographic coordinates, precise geospatial location information is assigned to each pixel point in the deformation rate map.

- Identification of Active Landslide Deformation Zones. Based on the deformation rate map, a reasonable deformation rate threshold is established and active landslide deformation zones are identified by comparing values against this threshold. Specifically:
 - i. Threshold Determination: The deformation rate threshold $\hat{\rho}$ is set by integrating the geological background of the study area, historical landslide deformation data, and monitoring accuracy requirements.
 - ii. Pixel-level screening: Iterate through all pixels in the deformation rate map and evaluate the deformation rate ρ_i for each pixel. If $|\rho_i| > \hat{\rho}$ holds, mark that pixel as a "potential active point."
 - iii. Spatial Clustering Analysis: Perform spatial clustering on marked potential active points (using the DBSCAN algorithm for density-based clustering with). Aggregate spatially contiguous or adjacent active points into regional units while removing isolated noise points.
 - iv. Identification of Active Deformation Zones: Combining topographic data with the clustered zones, boundaries are refined to exclude anomalies caused by non-landslide factors (e.g., deformation from man-made structures), thereby defining the spatial extent of active landslide deformation zones (landslide fracture development zones).

In this study, the parameter selection of DBSCAN algorithm was combined with the spatial distribution characteristics of landslide deformation in the research area and simulation testing. Through multiple experiments, it was determined that the neighborhood radius was set to 50 m to cover the reasonable spatial correlation range between adjacent pixel points in the active area of landslide deformation; The minimum number of points is set to 8 to ensure that the clustering area has sufficient deformation point density to distinguish between real active areas and noise. This parameter combination can effectively balance clustering integrity and noise removal effect.

2.3 Acquisition of morphological features of landslides and cracks based on UAV-based lidar point clouds

The spatial scope of active landslide deformation zones identified in Section 2.2 serves as prior constraint information for UAV LiDAR precision scanning. This approach aims to prevent indiscriminate detection across large areas, instead focusing on critical regions with developed fractures. By leveraging high-resolution 3D point cloud data from these zones, we capture morphological features such as crack width, depth, slope, and curvature, thereby establishing a foundation for subsequent extraction of landslide fracture edges. The specific procedure is described as follows:

1. UAV LiDAR point cloud data acquisition. The UAV-mounted LiDAR system emits laser pulses toward the target area (the active deformation zone identified in Section 2.2, i.e., the landslide fracture development zone). These pulses reflect off surface objects (landslide fractures) and return. By recording the round-trip time *t* of the laser pulses and

combining it with the speed of light v, the straight-line distance $L = (v \times t)/2L$ from the laser footprint to the UAV is calculated. Simultaneously, using the drone's POS (Position and Orientation System) data, obtain the precise position and orientation of the laser emission point. This determines the three-dimensional coordinates of the laser footprint in the global coordinate system, generating a high-density point cloud.

In the process of collecting LiDAR point cloud data from unmanned aerial vehicles, after calibration by professional measuring equipment and multiple repeated measurements, the horizontal accuracy root mean square error of the obtained point cloud was controlled within 0.05 m, and the vertical accuracy root mean square error was controlled within 0.03 m. This level of accuracy can effectively ensure the reliability and accuracy of the extracted landslide crack width, slope and other morphological features from the point cloud data.

- 2. 3D Modeling. Based on the point cloud data obtained in step (1), a 3D model of the landslide fracture zone is constructed. The specific process is as follows: First, preprocessing operations such as denoising, filtering, and simplification are performed on the acquired point cloud data to eliminate outliers and redundant data; Subsequently, the preprocessed high-density point cloud data is converted into a Triangulated Irregular Network (TIN) using the Delaunay triangulation algorithm. An interpolation algorithm then transforms the TIN into a high-resolution Digital Elevation Model (DEM). Finally, orthophotos are textured onto the 3D surface using texture mapping techniques based on the DEM. Lighting rendering technology is applied to enhance the visual impact of terrain undulations, ultimately generating a 3D model of the landslide fracture development zone.
- 3. Landslide fracture characteristic acquisition. Based on the generated three-dimensional model of the landslide fracture development zone, acquisition of landslide fracture characteristics are extracted. Given that landslide fractures exhibit characteristics such as narrow width, relatively continuous strike, varying depth, steep slope, and negative curvature, this study selected fracture width, strike, slope, and curvature index as landslide fracture features to describe fracture morphology using the 3D model. Specifically as follows Equation 15:

$$W = \sqrt{(X_B - X_A)^2 + (Y_B - Y_A)^2}$$
 (15)

a. Landslide Fracture Width: The vertical distance between rock and soil on both sides of the fracture in the horizontal direction, reflecting the tensile deformation of the landslide. Trends in width variation (e.g., wider in the middle, narrower at both ends) can indicate fracture propagation and stress concentration points (Sandric et al., 2024). In the 3D model of the landslide fracture zone, let O denote a point on the fracture centerline. Draw a horizontal line perpendicular to the fracture strike direction through this point. The intersection

points with the fracture boundaries on both sides are denoted as $A(X_A, Y_A)$ and $B(X_B, Y_B)$, respectively. The formula for the fracture width W at point O is:

For extracting the centerline of irregularly shaped cracks, a morphological skeleton based algorithm is adopted: firstly, the crack area in the 3D model is binary segmented, and the crack boundary pixels are gradually peeled off through continuous morphological erosion operations until only the central skeleton with a single pixel width is retained; For branching cracks, the distance transformation method is used to identify the local farthest point of each branch as the skeleton connection point, and the minimum spanning tree algorithm is used to optimize the skeleton topology structure; Finally, burrs and redundant branches are removed through skeleton trimming to generate a continuous centerline that conforms to the actual direction of the crack, ensuring the geometric accuracy of the direction calculation as follows Equation 16.

$$\alpha = \begin{cases} \arctan\left(\frac{Y_2 - Y_1}{X_2 - X_1}\right) \times \frac{180}{\pi} & (X_2 > X_1) \\ \arctan\left(\frac{Y_2 - Y_1}{X_2 - X_1}\right) \times \frac{180}{\pi} + 180^{\circ} (X_2 < X_1) \\ 90^{\circ} & (X_2 = X_1 \text{ and } Y_2 > Y_1) \\ 270^{\circ} & (X_2 = X_1 \text{ and } Y_2 < Y_1) \end{cases}$$
(16)

b. Slope Fracture Strike: The horizontal direction of fracture propagation, which is typically expressed as an angle relative to true north (ranging from 0° to 360°) and reflects the spatial distribution trend of fractures (Dias and Grohmann, 2024), aids in determining the movement direction and stress state of slope fractures. In the 3D model space of the landslide fracture zone, select two points along the fracture centerline: $G_1(X_1,Y_1)$ and $G_2(X_2,Y_2)$. The angle between the horizontal projection of the line connecting these two points and true north represents the fracture strike α . The formula is:

For landslide fractures with bends, segmented calculations of strike direction must be performed based on the spatial distribution of different fracture segments within the three-dimensional model space of the fracture development zone, with variation characteristics annotated accordingly as follows Equation 17.

$$p = \arctan\left(\sqrt{\left(\frac{\partial H}{\partial X}\right)^2 + \left(\frac{\partial H}{\partial Y}\right)^2}\right) \times \frac{180}{\pi}$$
 (17)

Where, *H* represents the elevation of point (X, Y), $\frac{\partial H}{\partial X}$ and $\frac{\partial H}{\partial Y}$ denote the slope rates of this point in the *X* and *Y* directions, respectively.

c. Landslide Fracture Slope: The inclination of fracture walls reflects the steepness of rock and soil on both sides of the fracture (Behley et al., 2021). Slope is determined by calculating the gradient change in elevation. For landslide fractures, their slope is often steeper than the surrounding terrain, serving as a key feature to distinguish fractured zones from normal topography. The formula for the slope of a fracture *p* at a point along the fracture edge line in the 3D model of the landslide fracture zone (*X*, *Y*) can be expressed as:

For the entire crack, the slope of all points along the edge line can be calculated and averaged to represent the overall slope characteristic of the crack as follows Equation 18.

$$\eta = \frac{1}{r} = \frac{4s}{abc} \tag{18}$$

Where, a, b and c represent the side lengths of the triangle formed by the point u(X, Y) and its two adjacent points on the fracture edge line, s represents the area of the triangle, r represents the radius of the triangle's circumcircle.

d. Slope Fracture Curvature: Indicates that the fracture edge exhibits a concave curvature toward the interior of the fracture, reflecting the bending characteristics of the fracture in its spatial distribution (Liu et al., 2025). This can assist in determining the stress state of the fracture. Within the three-dimensional model framework of the slope fracture development zone, for discrete point sequences, the curvature η of a point u(X, Y) can be expressed as:

Before constructing the Irregular Triangular Network (TIN), in order to filter overlapping point cloud data (data from vegetation and ground), a height threshold based method is used to set a reasonable height range according to the terrain characteristics of the landslide area. Point cloud data that exceeds this range (vegetation point cloud) and is below the reasonable lower limit (noise point cloud) are removed. At the same time, combined with point cloud intensity information, due to the difference in laser reflection intensity between vegetation and ground, the overlapping point cloud data from vegetation and ground are further screened by setting an intensity threshold to effectively filter out, avoid distortion of TIN construction, and ensure the accuracy of subsequent feature extraction.

The sign of curvature can be determined by the order of the three points: when the points are arranged clockwise along the crack's extension direction, the curvature is negative (concave toward the crack interior); when arranged counterclockwise, the curvature is positive (convex toward the crack exterior). For landslide cracks, the focus is typically on regions of negative curvature and their distribution characteristics.

By extracting features such as landslide fracture width, strike, slope, and curvature from, we obtain the morphological characteristics of landslide fractures. These are then used to construct the fracture feature vector $Q[W, \alpha, p, \eta]$.

For cracks with significant vertical undulations (stepped cracks), in order to avoid width calculation deviation caused by terrain undulations passing through non crack areas, the elevation normalization horizontal projection method is adopted: first, the elevation data of the crack centerline and boundary points on both sides are extracted, and the elevation of each point is normalized to the local reference plane (lowest point elevation) of the crack. Then, a horizontal projection line is generated on the normalized vertical profile to ensure that the measurement line always follows the actual extension direction of the crack and is not affected by terrain undulations, thus accurately calculating the true width of the crack.

2.4 Implementation of landslide extraction and fracture extraction

Based on the acquired landslide fracture feature vector *Q*, the probabilistic neural network (PNN) model is employed to extract landslide fractures, thereby obtaining their edge contours. The PNN model, a feedforward neural network, learns the probability density of data through training to calculate the probability of input samples belonging to different categories. It features fast training speed, high classification accuracy, and strong robustness against noisy data (Gui and Ma, 2025; L et al., 2024). When applied to landslide crack identification, it effectively handles complex nonlinear relationships in crack features, accurately distinguishing cracks from terrain undulations, vegetation cover, and other interfering features, enabling precise classification of landslide cracks pixels. The crack extraction process is as follows:

 PNN network model creation. Construct a four-layer PNN network model comprising input, pattern, accumulation, and output layers. The input layer receives feature vectors of target objects (landslide cracks); The pattern layer stores feature patterns of training samples (characteristics of landslide cracks versus non-cracked areas). It calculates similarity between input feature vectors and training sample patterns using radial basis functions, converting similarity into probability density values. The accumulation layer integrates outputs from the pattern layer. The output layer generates final classification results (crack/non-crack).

In PNN model training, the ratio of crack pixels to non crack pixels in the collected samples is about 1:5, with non crack samples dominating. To balance data distribution and avoid model bias towards non crack classification, oversampling techniques were adopted for crack samples. Specifically, SMOTE (Synthetic Minority oversampling Technique) algorithm was used to generate synthetic crack samples, and the ratio of crack and non crack samples was adjusted to 1:2, effectively improving the model's ability to recognize crack features.

2. Similarity Calculation and Probability Density Estimation. When a landslide fracture feature vector Q (originating from a specific location within the 3D model of the landslide fracture development zone) is input for classification, each neuron in the pattern layer calculates its similarity to the stored sample E using a Gaussian kernel function. It then outputs the probability density estimate $\ell_i(Q)$ indicating the likelihood of the input vector belonging to a particular category (fracture/non-fracture), expressed by the formula as follows Equation 19:

$$\ell_i(Q) = exp\left[-\frac{\|Q - E\|^2}{2\delta^2}\right]$$
 (19)

Where, δ represents the smoothing parameter, which controls the smoothness of the decision boundary.

In the construction of the 3D model in this study, after multiple experimental comparisons and actual requirement analysis, the grid cell size was determined to be 0.2 m. The optimization basis mainly lies in the fact that this size can retain key details of landslide cracks, such as subtle changes in crack direction and width differences,

to ensure the accuracy of crack extraction; It can also control the computational workload to a certain extent, avoiding a significant increase in computation time due to small unit sizes, which affects algorithm efficiency, and achieves a good balance between detail preservation and computational efficiency.

3. Category probability summation and decision. The accumulation layer sums the pattern layer's outputs by category, calculating the total probability density $\omega_g(Q)$ for the input feature vector Q belonging to the crack category g = 1 and the non-crack category g = 0 as follows Equation 20:

$$\omega_{g}(Q) = \sum_{i \in g} \mathcal{E}_{i}(Q) \tag{20}$$

The output layer assigns the input vector Q to the category with the maximum probability value based on Bayesian decision rules. Specifically, when $\omega_{g=1}(Q) > \omega_{g=0}(Q)$, the input Q is classified as belonging to the crack category (g=1); when $\omega_{g=1}(Q) < \omega_{g=0}(Q)$, it is classified as belonging to the non-crack category (g=0). This is expressed as follows Equation 21:

$$\hat{Y} = argmax \hat{\omega}_g(Q) \tag{21}$$

The classification result from the output layer (\hat{Y} , taking values of 1 or 0) determines whether the location is a landslide fracture.

- 4. Full-image scanning and probability map generation. The feature vectors of each grid cell in the 3D model of the landslide fracture development area in the study region are sequentially input into the trained PNN model to obtain the probability that each position belongs to a fracture, and a landslide fracture probability distribution map U(x, y) is generated. This probability map clearly reflects the possibility of a landslide fracture existing at each position in the study region.
- 5. Landslide fracture contour extraction. The Canny operator is used to extract the landslide fracture edge contour from the landslide fracture probability distribution map, which is described by the formula as follows Equation 22:

$$D_{edoe}(x,y) = U(x,y) * V(\sigma)$$
 (22)

In the formula, $D_{edge}(x,y)$ represents the image containing the fracture edge contour, $V(\sigma)$ represents a Gaussian filter with a standard deviation of σ .

To determine the high and low thresholds in Canny edge detection, the Otsu method is first used to perform preliminary threshold segmentation on the probability distribution map of landslide cracks, and obtain the basic threshold reference; Next, multiple sets of high and low threshold combinations are set near the basic threshold for testing. By comparing the integrity, continuity, and matching degree of the extracted crack edges with the actual cracks under different combinations, the optimal threshold combination that can maximize edge integrity and effectively suppress noise is finally selected.

In the constructed PNN network model, the number of input layer neurons is consistent with the dimension of the landslide crack feature vector; The number of neurons in the pattern layer is equal to the total number of training samples, and each neuron corresponds to a feature pattern of a training sample; The number of neurons in

TABLE 1 Main parameters of the experiment.

Name	Numerical value		
The degree of overlap of adjacent SAR images	>20%		
The central viewing angle of the main SAR image	35°-45°		
Vertical space baseline threshold	200 m		
Time baseline threshold	50days		
The incident Angle of radar waves	20°-50°		
Deformation rate threshold	10 mm/day		
Flight altitude of unmanned aerial vehicles	120 m		
The flight speed of unmanned aerial vehicles	8 m/s		
Radar scanning mode	Repeat scanning		
Smooth parameter	0.5		
Standard deviation of Gaussian filter	1.5		

the accumulation layer is the same as the number of classification categories, namely, crack and non crack categories; The output layer is a single neuron used to output the final classification result. This structure ensures the matching between model parameters and data size, avoiding overfitting or underfitting issues.

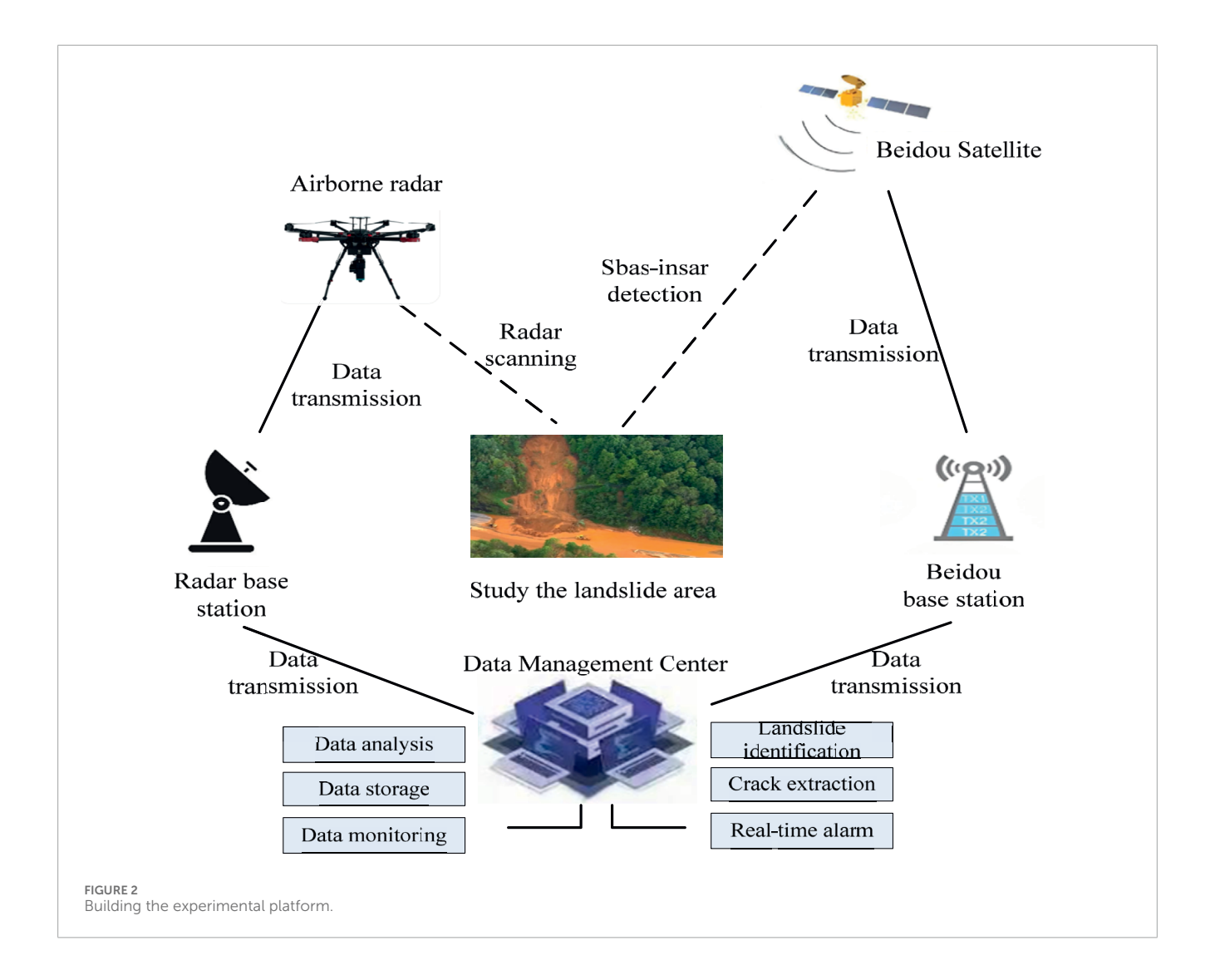
Through the above operations, the landslide fracture edge contour is obtained, and the landslide fracture extraction is realized.

3 Experimental analysis

To analyze the effectiveness of the landslide crack automatic extraction algorithm under InSAR UAV LiDAR point cloud coupling in this study, a typical landslide prone area in a county in Sichuan Province was selected as the experimental object. This area belongs to the southern section of the Longmenshan Fault Zone, with complex geological structures and mainly composed of weathered layers of Jurassic sandstone and mudstone. The surface is covered with a mixture of loose slope soil and strongly weathered rocks with a thickness of 2-8 m. According to the geological hazard survey data after the 2013 Lushan 7.0-magnitude earthquake, the historical landslide activity frequency in the study area reached 1.2 times per year. There are 17 existing landslide bodies with 23 tension, shear, and composite cracks developed, mainly in the NW-SE direction, with a width range of 0.3-2.1 m and a depth of 0.5-3.8 m. The rich landslide activity records and typical geological environmental characteristics in this area provide an ideal experimental field for verifying the adaptability of the algorithm under different geological conditions.

The primary experimental parameters for this study are listed in Table 1. The experimental platform constructed for practical needs is shown in Figure 2.

The deformation rate threshold is initially set based on the actual deformation rate of landslides in the historical landslide data of the

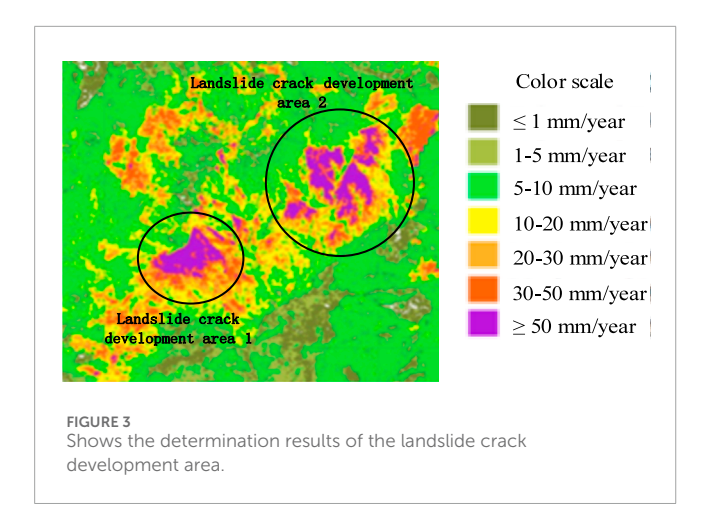


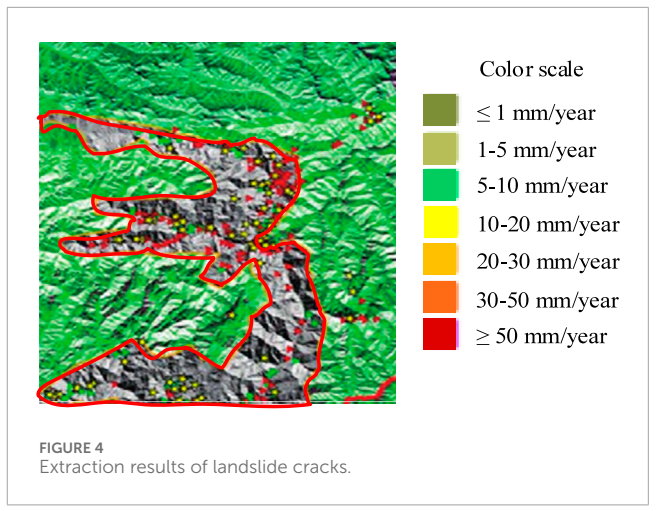
study area, combined with factors such as geological structure and soil characteristics of the area, and referring to previous landslide monitoring research experience under similar geological conditions. It is then adjusted through a small amount of preliminary testing. In this experiment, the drone's flight altitude was set to 120 m, based on a comprehensive balance between point cloud density and detection efficiency. After preliminary testing, the point cloud density at this altitude can reach 50–80 points per square meter, which can meet the recognition requirements of cracks at the 0.3 m level (with a spatial resolution of 0.15 m after Gaussian filtering), and can cover a research area of 8 square kilometers in a single flight. Although reducing the flight altitude can improve the point cloud density, it will significantly reduce the single operation range and increase the number of flights. After considering the scale characteristics of cracks and research efficiency, this parameter is determined.

Figure 2 Experimental platform utilizing BeiDou satellites, SBAS-InSAR detection technology monitors deformation in the study landslide area. Data is transmitted to BeiDou base stations and then to the data management center. Simultaneously, airborne radar scanned the same area, with data transmitted to the radar base station and then to the data management center. The center

integrated and analyzed the received data, combining macrodeformation information from InSAR with high-resolution 3D data from UAV LiDAR to precisely extract landslide cracks. Alarms were promptly issued based on the extraction results.

The experiment utilizes a constructed experimental platform to collect multi-scene terrain SAR imagery covering the target monitoring area over nearly 30 days using SBAS-InSAR technology. In the data collection process of this experiment, in order to ensure the consistency and correlation of the surface information reflected by InSAR and LiDAR data, they were basically synchronously collected. In the specific operation, InSAR data acquisition (using SBAS InSAR technology to collect multi scene terrain SAR images) and unmanned aerial vehicle LiDAR data acquisition are carried out within 24 h, minimizing the problem of data mismatch caused by changes in surface conditions due to time intervals, and ensuring the accuracy and reliability of landslide crack extraction results based on the fusion of the two types of data in the future. The imagery is arranged chronologically and undergoes radiometric calibration and multi-view processing. Following image registration, interferogram generation, phase unwrapping, error correction, and deformation inversion, the surface deformation rate for the area is obtained, generating a deformation rate map for





the region. Simultaneously, a reasonable deformation rate threshold was set. By comparing values against this threshold and integrating the DBSCAN clustering algorithm, active landslide deformation zones (landslide crack development areas) were identified. The experimental results are shown in Figure 3.

Figure 3 displays the deformation rate map of the target area, clearly distinguishing variations in deformation rates through distinct color coding. Among these, two areas predominantly colored purple were identified as landslide crack development zones, forming a stark contrast with the surrounding relatively stable areas appearing in green tones. This vivid color contrast clearly reflects that the surface deformation rates within the landslide crack development zones are higher than in the surrounding areas, indicating that these zones exhibit a significant landslide deformation trend and are key areas for landslide crack development. From a technical perspective, the SBAS-InSAR technology employed in this study precisely captures subtle surface deformation information through the processing and analysis of multi-scene SAR imagery. The spatial distribution of development zones and color gradients in Figure 3 not only demonstrate the technology's high sensitivity to landslide deformation but also provide reliable and critical deformation rate data for delineating active landslide deformation zones. Furthermore, this technology effectively identifies potential hotspots for landslide crack development. It establishes a clear prior constraint range for subsequent detailed UAV LiDAR point cloud scanning and automated landslide crack extraction, significantly enhancing the precision and efficiency of landslide crack monitoring.

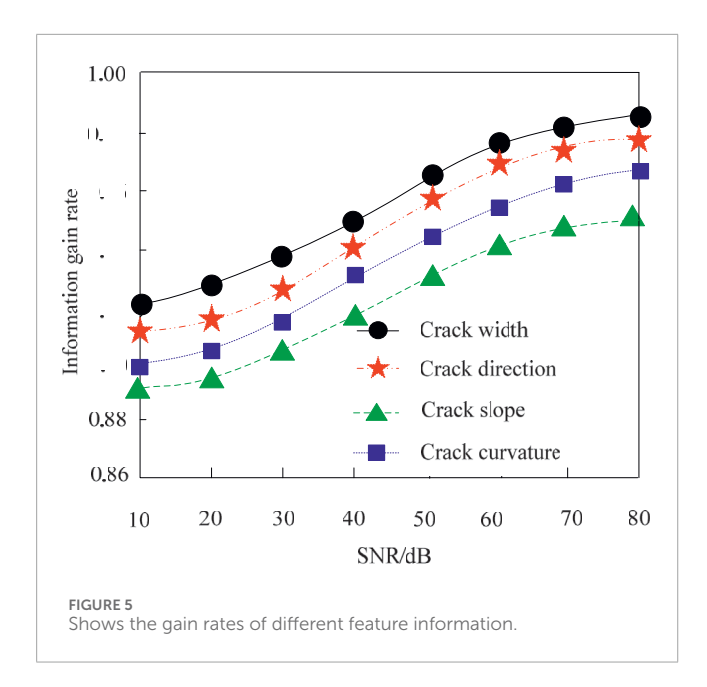
Then, UAV LiDAR technology was employed to scan identified landslide fracture development zones, collecting point cloud data for three-dimensional modeling. From this, morphological features such as fracture width, strike, dip, and curvature were extracted to construct a landslide fracture feature vector. The feature vector was input into a pre-built four-layer PNN model. This model outputs the probability that a point belongs to a landslide crack, generating a crack probability distribution map. Subsequently, the Canny edge detector was applied to extract crack edge contours, achieving automated landslide crack extraction. Selected extraction results are shown in Figure 4.

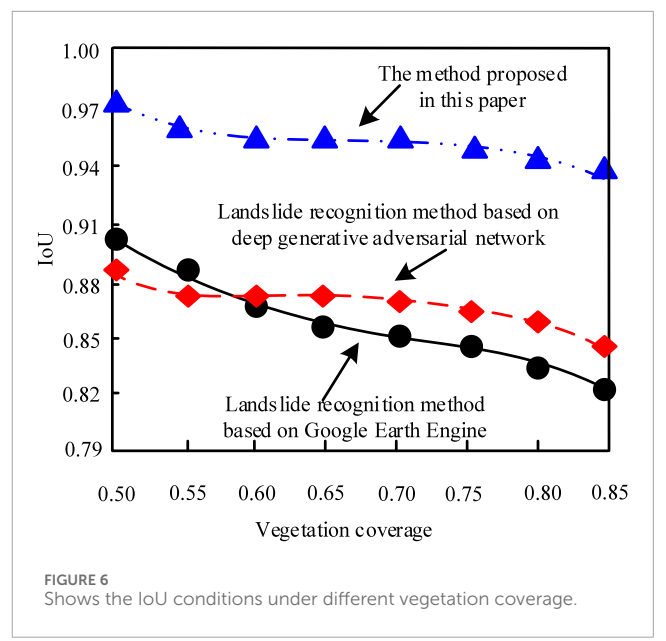
As shown in Figure 4, the red lines clearly delineate the crack edge contours extracted by the proposed algorithm. In

terms of distribution, the cracks exhibit irregular morphology with distinct extensions and turns across different regions, reflecting the complexity and diversity of landslide cracks in actual terrain. Simultaneously, features such as crack width, strike, slope, and curvature extracted from the 3D model constructed from point cloud data are indirectly reflected in the crack morphology within the figure. For instance, wider sections may correspond to areas with more intense landslide activity. Furthermore, the results in Figure 4 obtained using this algorithm fully validate the effectiveness and advantages of UAV LiDAR technology in landslide crack extraction. High-precision point cloud data acquisition and 3D modeling accurately capture subtle morphological features of cracks, providing a reliable data foundation for constructing landslide crack feature vectors. The application of a four-layer PNN model effectively handles the complex nonlinear relationships of crack features, accurately outputting the probability of each point belonging to a landslide crack. Subsequently, the Canny edge detection algorithm successfully extracts crack edge contours, achieving automated landslide crack extraction. These results not only visually depict the distribution patterns of landslide fractures and precisely locate their spatial positions but also provide intuitive and critical information for in-depth analysis of fracture development patterns and assessment of landslide stability. This holds significant importance for establishing a comprehensive realtime monitoring and early warning system for landslide disasters.

For the method presented in this paper, the extraction of morphological features of landslide fractures is crucial, as it directly impacts the reliability of fracture edge extraction. To address this, the experiment employs the information gain rate metric to evaluate the contribution value of four selected features-slope crack width, strike, dip, and curvature-to the target task of slope crack extraction. The information gain rate measures the informational contribution of features to classification tasks, with values ranging from [0,1]. For automated landslide crack extraction, higher values indicate greater value for the task. Test results are shown in Figure 5.

As illustrated in Figure 5, the trend of different feature information gain rates with signal-to-noise ratio (SNR) reveals that crack width consistently maintains the highest information gain rate across all SNR ranges, peaking at 0.98. It also performs exceptionally well at lower SNRs (10–30 dB), demonstrating strong





robustness against noise. This feature effectively distinguishes landslide cracks from normal terrain, providing the model with the most stable and discriminative morphological basis. Crack orientation and slope information yield the next highest gain rates. In contrast, the information gain rate for crack curvature consistently lagged behind the other three features, showing a smaller increase. This indicates its limited discriminatory capability for landslide crack extraction and relatively minor contribution. This is attributed to curvature features being susceptible to local noise interference and their insufficient discriminative significance in morphological representation. Nevertheless, it maintains a high overall level, with an information gain rate exceeding 0.89. This feature selection did not include crack depth mainly because the use of unmanned aerial vehicle LiDAR to measure crack depth is limited by equipment accuracy and complex terrain conditions, resulting in large measurement errors and difficulty in accurately obtaining depth information. Therefore, it was not included as a feature. Overall, the information gain rates of all four morphological features increased with improved signal-to-noise ratio (SNR). This indicates that enhanced data quality strengthens each feature's informational contribution to landslide crack extraction, enabling more thorough exploitation of their discriminative value. From a feature selection perspective, all four features make significant contributions to landslide crack extraction. Specifically, crack width and orientation should be prioritized as key features in extraction models, while slope and curvature serve as effective supplements. Together, they form a robust, comprehensive feature set that enhances the model's overall extraction performance across varying signal-to-noise ratio conditions.

Intersection over Union (IoU) refers to the ratio of the intersection area between the landslide crack area extracted by the algorithm and the actual crack area (true value) to the union area, which can reflect the accuracy of the landslide crack extraction results and the degree of regional matching. When the IoU value approaches 1, it indicates that the extracted crack area coincides with the actual area in height, and the extraction algorithm is effective and

accurate; On the contrary, when the IoU value is low, it indicates that there is a significant deviation between the extracted results and the actual situation. Fifty independent test cases were selected for the experiment, covering various types of landslides such as shallow soil landslides and rock landslides. The performance of our algorithm was evaluated using this indicator, and compared and analyzed with Khadka et al.'s landslide recognition method based on Google Earth Engine in 2025 and Lekshmana and George's landslide recognition method based on deep generative adversarial networks in 2023. The results are shown in Figure 6.

As shown in the IoU performance comparison in Figure 6, it is clearly observable that the proposed algorithm consistently maintains the highest IoU values across the entire range of vegetation coverage variations. Its curve exhibits the greatest stability with the smallest fluctuation amplitude, with an overall level exceeding 0.94. This demonstrates the proposed algorithm's strong robustness against vegetation occlusion interference, effectively overcoming challenges such as complex textures and blurred features caused by vegetation coverage. It accurately matches actual fracture areas, achieving superior and stable extraction accuracy. In contrast, the IoU values of the Landslide recognition method based on Google Earth Engine and the Landslide recognition method based on deep generative adversarial network both show a significant downward trend with increasing vegetation coverage, especially under moderate to high vegetation coverage conditions where performance degradation is significant. This indicates that these two methods are more sensitive to vegetation environments, and their feature extraction and spatial analysis capabilities are limited in complex scenarios, making it difficult to effectively distinguish vegetation noise from real crack features. Overall, the proposed algorithm demonstrates higher accuracy and regional matching capability across diverse vegetation coverage environments, validating its effectiveness and advanced performance in complex natural settings.

To further validate the performance superiority of the InSAR unmanned aerial vehicle LiDAR point cloud coupled landslide

TABLE 2 Comparison of algorithm performance under different landslide types and Gaussian filter standard deviation.

Landslide	Evaluation metrics	The method proposed in this paper			Landslide	Landslide
type		Standard deviation 1.0	Standard deviation 1.5	Standard deviation 2.0	recognition method based on google earth engine	recognition method based on deep generative adversarial network
Gentle landslide	Accuracy (%)	95.2	94.8	93.5	88.6	85.3
	Recall rate (%)	93.8	94.2	92.7	86.4	83.1
	F1 score	94.5	94.5	93.1	87.5	84.2
	Edge smoothness (pixels)	2.1	2.3	2.5	3.8	4.2
	Running time (s)	12.5	13.2	14.0	18.7	20.3
Shallow soil landslide	Accuracy (%)	94.7	94.3	93.0	87.9	84.7
	Recall rate (%)	93.3	93.7	92.2	85.8	82.6
	F1 score	94.0	94.0	92.6	86.8	83.6
	Edge smoothness (pixels)	2.3	2.4	2.6	3.9	4.3
	Running time (s)	13.0	13.7	14.5	19.2	20.8
Rock landslide	Accuracy (%)	95.5	95.0	93.8	89.1	85.8
	Recall rate (%)	94.1	94.5	93.0	86.9	83.5
	F1 score	94.8	94.7	93.4	88.0	84.6
	Edge smoothness (pixels)	2.0	2.2	2.4	3.7	4.1
	Running time (s)	12.0	12.7	13.5	18.2	19.8

crack automatic extraction algorithm proposed in this paper under different landslide types and Gaussian filter standard deviations (1.0, 1.5, 2.0), another typical slow-moving landslide area in Sichuan Province was selected as the experimental object, and compared with the Landslide recognition method based on Google Earth Engine and the Landslide recognition method based on deep generative adversarial network. And use precision (to avoid false positives), recall (to avoid missed detections), F1 score, edge smoothness, and running time as evaluation metrics. The experimental results are shown in Table 2.

According to Table 2 analysis, it can be seen that the algorithm proposed in this paper has significant performance advantages under different landslide types and Gaussian filter standard deviation conditions. In terms of accuracy, whether it is slow-moving landslides, shallow soil landslides, or rock landslides, the algorithm in this paper far exceeds the Landslide recognition method based on Google Earth Engine and the Landslide recognition method based on deep generative adversarial network at standard deviations of 1.0, 1.5, and 2.0. The highest accuracy

reaches 95.5%, indicating that the algorithm in this paper can effectively avoid false alarms and accurately identify landslide cracks. In terms of recall rate, the algorithm presented in this article also performs outstandingly, outperforming the compared algorithms in various landslide types and standard deviation settings, indicating that it can effectively avoid missed detections and ensure that more real cracks are identified. As a comprehensive indicator of accuracy and recall, the F1 score of this algorithm maintains a high level, up to 94.8%, under three types of landslides and different standard deviations, further proving its superior comprehensive performance. The edge smoothness index shows that the crack edges extracted by the algorithm in this article are smoother, with significantly lower pixel values than the comparison algorithm, indicating higher quality of the extracted results. In terms of running time, the algorithm in this article is shorter than the comparative algorithm under all conditions, reflecting its efficiency. Overall, the algorithm presented in this article demonstrates higher accuracy, comprehensiveness, result quality, and operational efficiency under different landslide types and Gaussian filter standard deviations,

demonstrating significant performance advantages. In addition, different standard deviations of Gaussian filters have a certain impact on algorithm performance. In terms of edge smoothness, as the standard deviation increases from 1.0 to 2.0, the pixel values of edge smoothness extracted by our algorithm and the comparison algorithm show an upward trend. This indicates that as the standard deviation increases, the smoothing effect of the filtering process on the point cloud data is enhanced, resulting in a change in edge smoothness. However, when the standard deviation is set to 1.5, the algorithm proposed in this paper still significantly outperforms the Landslide recognition method based on Google Earth Engine and deep generative adversarial network in terms of edge smoothness index while ensuring high accuracy and recall. Moreover, the F1 score of the algorithm is at a high level for the three types of landslides, indicating that under this standard deviation, the algorithm can effectively smooth the edges while maintaining crack features, ensuring the accuracy of extraction and verifying the rationality of parameter selection.

4 Conclusion

In recent years, the integration of multi-source technologies has provided novel solutions for landslide monitoring. This study proposes an InSAR-UAV LiDAR point cloud coupled algorithm for automatic landslide crack extraction. By establishing a "macro-localization-fine-extraction" collaborative framework that integrates SBAS-InSAR technology with UAV LiDAR technology, the algorithm achieves efficient and precise automatic extraction of landslide cracks. The algorithm's core lies not in merely juxtaposing results from both technologies, but in an implicit sequential logic: using SBAS-InSAR-derived macroscopic deformation zones to guide and focus LiDAR's detailed crack extraction (i.e., pinpointing cracks within active zones). This "area-to-point," "macro-to-micro" guidance relationship constitutes the essence of their coupling. It avoids the imprecision of using InSAR alone for large-scale deformation analysis and the inefficiency of employing LiDAR solely for global scanning. Experimental results demonstrate that this algorithm significantly enhances crack extraction accuracy, enabling precise identification of narrow, fine cracks. It exhibits strong robustness, operating stably across landslide areas with varying terrain complexity and delivering reliable extraction results. However, although this algorithm has shown significant effectiveness in extracting landslide cracks, it also has certain limitations. For example, in heavy rainfall environments, rapid changes in surface conditions may interfere with the deformation monitoring of InSAR technology, affecting the accuracy of macroscopic positioning; In dense forest areas with poor LiDAR penetration, it is difficult to obtain effective point cloud data, which limits the fine extraction of cracks. Future work will focus on optimizing the algorithm to adapt to complex weather conditions, developing special data processing methods for dense vegetation areas, and exploring integration with other emerging technologies to further enhance the universality and reliability of algorithms.

Data availability statement

The original contributions presented in the study are included in the article/supplementary material, further inquiries can be directed to the corresponding author.

Author contributions

KD: Conceptualization, Resources, Writing – original draft, Writing – review and editing. BY: Data curation, Investigation, Methodology, Writing – original draft, Writing – review and editing. ZY: Methodology, Supervision, Writing – original draft. QP: Conceptualization, Formal Analysis, Validation, Writing – original draft. LH: Data curation, Methodology, Visualization, Writing – review and editing.

Funding

The author(s) declare that no financial support was received for the research and/or publication of this article.

Conflict of interest

Author BY was employed by Southwest Company of China Airport Planning and Design Institute Co., Ltd. Author ZY was employed by Chengdu Engineering Consulting Co., Ltd.

The remaining authors declare that the research was conducted in the absence of any commercial or financial relationships that could be construed as a potential conflict of interest.

Generative Al statement

The author(s) declare that no Generative AI was used in the creation of this manuscript.

Any alternative text (alt text) provided alongside figures in this article has been generated by Frontiers with the support of artificial intelligence and reasonable efforts have been made to ensure accuracy, including review by the authors wherever possible. If you identify any issues, please contact us.

Publisher's note

All claims expressed in this article are solely those of the authors and do not necessarily represent those of their affiliated organizations, or those of the publisher, the editors and the reviewers. Any product that may be evaluated in this article, or claim that may be made by its manufacturer, is not guaranteed or endorsed by the publisher.

References

Behley, J., Garbade, M., Milioto, A., Quenzel, J., Behnke, S., Gall, J., et al. (2021). Towards 3d lidar-based semantic scene understanding of 3d point cloud sequences: the semantickitti dataset. *Int. J. Robotics Res.* 40 (8/9), 959–967. doi:10.1177/02783649211006735

Devaraj, S., Yarrakula, K., Martha, T. R., Murugesan, G. P., Vaka, D. S., Surampudi, S., et al. (2022). Time series sar interferometry approach for landslide identification in mountainous areas of Western ghats, India. *J. Earth Syst. Sci.* 131 (2), 133–17. doi:10.1007/s12040-022-01876-3

Dias, H. C., and Grohmann, C. H. (2024). Standards for shallow landslide identification in Brazil: spatial trends and inventory mapping. *J. S. Am. Earth Sci.* 135 (Mar), 104805–1.10. doi:10.1016/j.jsames.2024.104805

Diels, L., Vlaminck, M., Wit, B. D., Philips, W., and Luong, H. (2022). On the optimal mounting angle for a spinning lidar on a uav. *IEEE Sensors J.* 22 (21), 21240–21247. doi:10.1109/jsen.2022.3208434

Gui, S. Y., and Ma, S. Q. (2025). Simulation of multi Echo Lidar topographic mapping in downhill areas of highways. $Comput.\ Simul.\ 42$ (4), 162-165+445.

Khadka, D., Zhang, J., and Sharma, A. (2025). Geographic object-based image analysis for landslide identification using machine learning on google earth engine. *Environ. Earth Sci.* 84, 92. doi:10.1007/s12665-024-12045-8

Liu, Z. J., Qiu, H. J., Zhu, Y. R., Huang, F. W. Ch., Ye, B. F., Wei, Y. D., et al. (2024). Increasing irrigation-triggered landslide activity caused by intensive farming in deserts on three continents. *Int. J. Appl. Earth Observation Geoinformation* 134, 104242. doi:10.1016/j.jag.2024.104242

Lekshmanan, L., and George, A. S. S. (2023). Landslide identification using water cycle particle swarm optimization-based deep generative adversarial network. *Concurrency and Comput. Pract. and Exp.* 35 (8), e7617–e7617.14. doi:10.1002/cpe.7617

Liu, B. J., Wu, X. S., Zhang, X. Y., Fang, Y. F., Ge, R. W., and Li, Q. (2025). Development of low frequency acoustic sensor for rock and soil mass motion measurement. *Chin. J. Sensors Actuators* 38 (3), 377–386.

Mahesh, T., Neeraj, K., Kiran, D. R., and Malik, J. N. (2023). Geological and geotechnical investigations of the sataun landslide along the active sirmauri tal fault, sataun, northwestern himalaya, India. *Landslides* 20 (5), 1045–1063. doi:10.1007/s10346-023-02038-2

Ozturk, U. (2022). Geohazards explained 10: time-dependent landslide susceptibility. Geol. Today 38 (3), 117–120. doi:10.1111/gto.12391

Qadami, B. S. A., Oujidi, M., Ejjaouani, H., and Okaishi, W. A. (2023). A study of network roads landslides and their stabilization methods in fahs anjra province: north of Morocco. *Indian Geotechnical J.* 53 (3), 593–612. doi:10.1007/s40098-022-00696-y

Qiu, H. J., Li, Y. J., Zhu, Y. R., Ye, B. F., Yang, D. D., Liu, Y., et al. (2025). Do post-failure landslides become stable? *CATENA* 249, 108699. doi:10.1016/j.catena.2025.108699

Sandric, I., Chitu, Z., Ilinca, V., and Irimia, R. (2024). Using high-resolution uav imagery and artificial intelligence to detect and map landslide cracks automatically. *Landslides* 21 (10), 2535–2543. doi:10.1007/s10346-024-02295-9

Sari, P. T. K., Mochtar, I. B., and Lastiasih, Y. (2024). Special case on landslide in balikpapan, Indonesia viewed from crack soil approach. *KSCE J. Civ. Eng.* 28 (6), 2173–2188. doi:10.1007/s12205-024-0402-3

Shameem, A. A., Sudha, S., and Francis, S. (2022). Identification and classification of landslide susceptible zone using geospatial techniques and machine learning models. *Geocarto Int.* 37 (27), 18328–18355. doi:10.1080/10106049.2022.2138986

Tebbouche, M. Y., Ait Benamar, D., Hassan, H. M., Singh, A. P., Bencharif, R., Machane, D., et al. (2022). Characterization of el kherba landslide triggered by the August 07, 2020, mw=4.9 mila earthquake (algeria) based on post-event field observations and ambient noise analysis. *Environ. Earth Sci.* 81 (2), 46–16. doi:10.1007/s12665-022-10172-8

Tiwari, A., Tewari, M., Pathak, K., and Mandal, B. B. (2024). Analysis of *in-situ* creep behavior of coal mine waste dumps using gbinsar for landslide failure prediction. *Min. Metallurgy and Explor.* 41 (5), 2511–2523. doi:10.1007/s42461-024-01077-0

Yamaguchi, S., and Kasai, M. (2022). A new index representative of seismic cracks to assess post-seismic landslide susceptibility. *Trans. GIS TG* 26 (2), 1040–1061. doi:10.1111/tgis.12900

Yang, G. Q., Qiu, H. J., Wang, N. L., Yang, D. D., and Liu, Y. (2025). Tracking 35-year dynamics of retrogressive thaw slumps across permafrost regions of the Tibetan Plateau. *Remote Sens. Environ.* 325, 114786. doi:10.1016/j.rse.2025.114786

Yunus, A. P., Sajinkumar, K. S., Gopinath, G., Subramanian, S. S., Kaushal, S., Thanveer, J., et al. (2025). Chronicle of destruction: the wayanad landslide of July 30, 2024. *Landslides* 22, 1891–1908. doi:10.1007/s10346-025-02494-y